

# A NEURAL NETWORK-BASED OBSERVATION OPERATOR FOR WEATHER RADAR DATA ASSIMILATION

Marco Stefanelli<sup>1</sup>, Žiga Zaplotnik<sup>2,1</sup>, Gregor Skok<sup>1</sup>

<sup>1</sup>University of Ljubljana, Faculty of Mathematics and Physics,  
Jadranska Cesta 19, 1000 Ljubljana, Slovenia

<sup>2</sup>European Centre for Medium-Range Weather Forecasts,  
Robert-Schuman-Platz 3, 53175 Bonn, Germany

Corresponding author: Marco Stefanelli  
[marco.stefanelli@fmf.uni-lj.si](mailto:marco.stefanelli@fmf.uni-lj.si)

---

## Abstract

In three-dimensional variational data assimilation (3DVar) for numerical weather prediction (NWP), the observation operator  $\mathcal{H}$  plays a central role by mapping model state variables to an observation equivalent. For weather radar, however, specifying  $\mathcal{H}$  is particularly challenging: reflectivity is a nonlinear, microphysics-dependent diagnostic quantity that only indirectly relates to the model's prognostic variables, making traditional parameterised radar operators complex, regime-dependent and difficult to tune.

In this study, we propose a neural-network (NN)-based observation operator for radar reflectivity and apply it within a 3DVar data assimilation (DA) framework. Using five years (2019–2023) of radar reflectivity data from the Lisca radar and 4.4 km-resolution short-range forecasts from ALADIN model over Slovenia, we train a convolutional encoder–decoder neural network to map model temperature, humidity, horizontal wind components and surface pressure fields to radar reflectivity. Across independent test cases spanning clear-sky, stratiform and convective regimes, the NN-based operator accurately reproduces the spatial structure and intensity of observed reflectivity, relying primarily on the model state in the vicinity of the observation point. In the extreme precipitation case, which caused widespread floods in Slovenia on August 4, 2023, assimilating the full radar disc reduces the domain-averaged reflectivity root-mean-square error (RMSE) from 5.99 dBZ to 3.47 dBZ and improves the alignment between the analysed and observed convective bands.

Embedded within 3DVar, the Jacobian of the NN observation operator allows radar reflectivity observations to inform model state variables, producing corresponding analysis increments. The proposed NN radar observation operator offers a flexible alternative to traditional parameterised radar operators for improving convective-storm forecasts.

**Keywords:** Data Assimilation, Observation Operator, Neural Network Observation Operator, Radar Data Assimilation,

---

## 1. Introduction

Recent years have witnessed growing interest in hybrid approaches that integrate machine learning (ML) techniques into traditional data assimilation (DA) frameworks, aiming to overcome structural and computational limitations in geophysical DA systems (e.g. see [Cheng et al. \(2023\)](#) and ([Pasmans et al., 2025](#)) for a comprehensive review). ML methods have been successfully used to reformulate complex components of DA systems, such as background error covariance modelling ([Melinec and Zaplotnik, 2024](#); [Melinec et al., 2025](#)) or the observation operator for coupled ocean–acoustic variational data assimilation ([Storto et al., 2021](#)). These developments suggest that ML can learn nonlinear relationships that are difficult to express analytically or to parameterise within classical statistical frameworks.

Among the various DA applications, radar data assimilation (DA) presents unique challenges. Despite the high spatial and temporal resolution of radar observations, their assimilation into numerical weather prediction (NWP) models remains problematic ([Fabry and Meunier, 2020](#)). Numerous variational and ensemble-based techniques have been developed to assimilate radar reflectivity and doppler velocity data (e.g., [Stephan et al., 2008](#); [Dowell et al., 2011](#); [Wattrelot et al., 2014](#); [Liu et al., 2020](#); [Thiruvengadam and Ghosh, 2021](#)), yet the improvement in short-term convective forecasts remains limited.

As emphasised by [Fabry and Meunier \(2020\)](#), radar DA faces a fundamental representativeness problem. Precipitation fields exhibit intense small-scale variability and strong nonlinearity, which are only partially resolved by current NWP systems. This leads to systematic mismatches between observed and simulated radar reflectivity, especially at convective scales, where unresolved structures and imperfect microphysical parameterisations dominate errors ([Fabry and Meunier, 2020](#)). Consequently, simple extrapolation methods for radar nowcasting often outperform numerical forecasts with radar DA during the first few hours (FIG. 1 in [Fabry and Meunier, 2020](#)). These difficulties originate from a combination of model and system-related factors. On the modelling side, limited spatial resolution and simplified microphysical and convection schemes prevent the NWP model from representing the fine-scale variability captured by radar observations. On the DA side, the observation operator plays a critical role as the translator between model and observation spaces. When this operator, together with the underlying model physics, cannot reproduce radar reflectivity for the correct meteorological reasons, the innovations lose their physical meaning. As a result, the assimilation process may introduce corrections that do not accurately reflect the actual atmospheric state, thereby reducing the effectiveness of the analysis. Furthermore, in most current operational systems, the assimilation of radar reflectivity primarily corrects the hydrometeor or precipitation fields, with limited or no adjustment to the dynamical and thermodynamical variables (e.g., temperature, humidity, horizontal wind components). These corrections tend to decay rapidly during model integration, limiting their predictive value ([Fabry and Meunier, 2020](#)).

These limitations highlight the central role of the observation operator in determining the effectiveness of radar DA. Because it bridges the model and observation spaces, any structural inadequacy in the operator, such as oversimplified microphysics or nonlinear scattering relationships, directly constrains the physical consistency of the analysis. Conventional radar operators, which rely on parameterised descriptions of hydrometeor backscattering, are not only computationally demanding but also highly sensitive to assumptions about hydrometeor particle size distributions and scattering properties. As a result, they often struggle to reproduce observed reflectivities for the right physical reasons, reinforcing the representativeness problem described above.

These challenges underscore the need for a more flexible formulation of the radar observation operator. We propose a neural-network (NN)-based observation operator designed to learn the nonlinear mapping between dynamical and thermodynamic model state variables (temperature, humidity, wind components, and pressure) and radar reflectivity. This data-driven operator is embedded within a variational DA framework to improve the realism and efficiency of the forward process, ultimately enhancing the representativeness of innovations and the impact of

radar DA on convective-scale forecasts.

The paper is organised as follows. Section 2 presents methodological aspects of our study, Section 3 presents the results. Discussion and Conclusions are given in Section 4.

## 2. Methodology

In this study, we propose an NN-based observation operator for weather radar reflectivity and apply it in a 3DVar data assimilation. The NN observation operator is trained to map short-range forecasts of temperature ( $t$ ), horizontal wind components ( $u$  and  $v$ ), relative humidity ( $r$ ), at four pressure levels (975 hPa, 925 hPa, 850 hPa, and 800 hPa) and three surface variables, 2 m temperature ( $t2m$ ), 2 m relative humidity ( $r2m$ ) and mean sea level pressure ( $msl$ ) from the ALADIN numerical weather prediction model (hereafter 'ALADIN model outputs' refers to the listed fields) to the corresponding observed radar reflectivities. Once trained, the NN observation operator is used in 3DVar to produce model-equivalent of radar reflectivities and tested for independent cases not included in the training dataset.

In this section, we first describe the radar and model datasets used to construct and evaluate the NN operator (Section 2.1: Dataset description). We then summarise the 3DVar formulation and its configuration for the present study (Section 2.2: 3DVar formulation). The architecture and implementation of the NN-based observation operator are detailed in Section 2.3: The NN Observation Operator. Finally, the training strategy is presented in Section 2.4: Training setup.

### 2.1. Dataset description

To develop the proposed NN observation operator, we used five years (2019–2023) of ALADIN model outputs and weather radar data from the Lisca radar (Slovenia, 46.07°N, 15.29°E, 945 m a.s.l., frequency band: C, [Stržinar and Skok \(2018\)](#); further details at [World Meteorological Organization \(Lisca wgs84\)](#), 2025), both provided by the Slovenian Met Office (ARSO). The ALADIN model ([Termonia et al., 2018](#)) data were available at a horizontal resolution of 4.4 km and a temporal resolution of 1 h and 6 h lead time, with a 6 h analysis cycle (00, 06, 12, 18 UTC). From the radar dataset, we selected the lowest elevation angle (0.5°) and computed the 3-D coordinates ( $x$ ,  $y$ ,  $z$ ) using the Python package *xradar* ([Grover et al., 2025](#)) which refers to [Doviak and Zrnic \(2014\)](#) for mathematical formulation. Both the ALADIN and radar domains are shown in Fig. 1. Red areas on the radar disc indicate regions where the radar beam is blocked by terrain, i.e. the mountain shadow zones. These occur mostly to the northwest in the lee of the Kamnik-Savinja Alps.

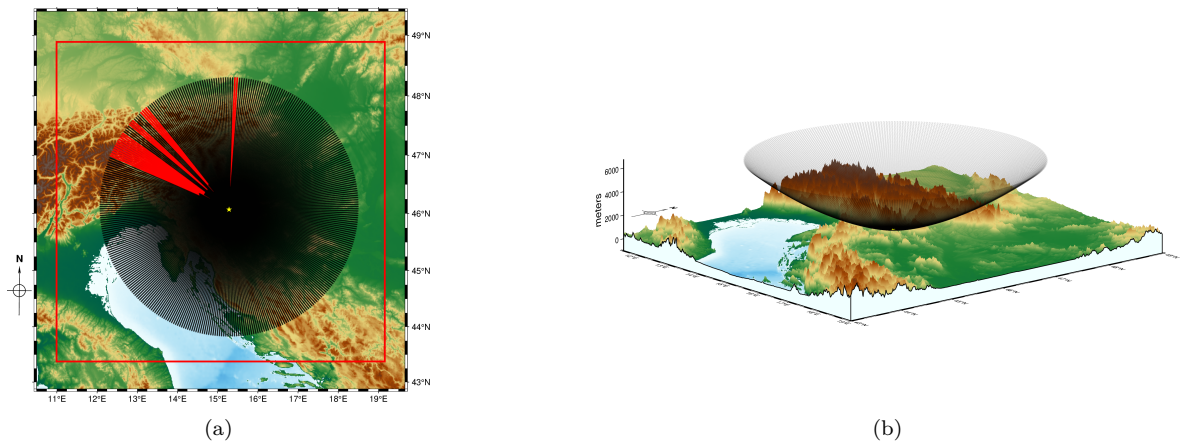


Figure 1: Spatial overview of the datasets used for training the neural-network observation operator. (a) spatial domain and radar sampling. The red square indicates the spatial extent of the ALADIN data used in the analysis, and the black dots indicate the coverage of the Lisca radar of 0.5° elevation. Red areas on the radar disc indicate regions where terrain mountain shadow zones block the radar beam. (b) 3D geometry of the Lisca radar's first elevation scan (0.5°).

Before their use in model training, radar reflectivity data were preprocessed to ensure temporal and spatial consistency, as well as overall data quality. Following the operational quality-control procedures used at Slovenian Met Office, two filters were applied: (1) only observations within a 160 km horizontal radius of the radar site were retained, which corresponds to roughly the first 3 km of the atmospheric column, and (2) reflectivity values below 13.5 dBZ were discarded and set to NaN to suppress background noise and spurious echoes.

To further enhance data quality, a global outlier mask was constructed using a histogram-based Mahalanobis distance approach as in [Franch et al. \(2020\)](#). For each radar resolution gate (i.e. each fixed position in the azimuth–range radar grid), we constructed a normalised histogram of reflectivity using 526 bins of width 0.1 dBZ, based on a random subset comprising 20% of all available time steps. Each gate’s histogram was then treated as a feature vector in an  $N_{\text{bins}}$ -dimensional space. Using all gates, we estimated the global mean histogram and covariance matrix, and subsequently computed the Mahalanobis distance for each gate  $i$  as follows:

$$D_i = \sqrt{(\mathbf{x}_i - \boldsymbol{\mu})^T \boldsymbol{\Sigma}^{-1} (\mathbf{x}_i - \boldsymbol{\mu})}, \quad (1)$$

In Eq. (1),  $\mathbf{x}_i$  denotes the histogram vector at gate  $i$ ,  $\boldsymbol{\mu}$  is the global mean histogram vector, and  $\boldsymbol{\Sigma}$  is the covariance matrix of all gates. To ensure numerical stability, a small regularisation term ( $\varepsilon = 10^{-6}$ ) was added to the diagonal of  $\boldsymbol{\Sigma}$  prior to inversion. Gates with distances exceeding the 90th percentile threshold (i.e., the upper 10% of the distribution) were classified as outliers. The resulting mask (Fig. 2) was then applied to remove these outlier gates from the dataset. A strong spatial correspondence is observed between the outlier mask derived from the Mahalanobis distance analysis (Fig. 2) and the terrain-induced radar beam blockage areas (Fig. 1-a). This correlation suggests that a significant fraction of the identified outliers originates from regions affected by partial or complete signal obstruction by mountainous terrain, highlighting the method’s sensitivity to detecting physically meaningful artefacts in the radar observations.

The practical impact of the cleaning procedures is illustrated in Fig. 3, which shows a representative example of the raw radar field (Fig. 3-a), the cleaned dataset (Fig. 3-b), and the corresponding difference map (Fig. 3-c), highlighting the filtered points. The raw data exhibit numerous radial streaks and azimuth–range sectors contaminated by non-meteorological echoes, many of which coincide with regions of known beam blockage. After applying the radial filter and the Mahalanobis-based outlier mask, these artefacts are effectively removed, yielding a spatially coherent precipitation field with substantially reduced noise. The difference panel highlights the removed gates in red tones.

The quality-controlled radar observations were subsequently summed into 1-hour intervals to match the temporal resolution of the ALADIN model outputs. Furthermore, they were spatially interpolated onto the model grid (by taking the value from the nearest radar point) to ensure spatial consistency between the two datasets. Finally, since radar observations have some missing timesteps, to maintain temporal coherence, the ALADIN dataset was filtered to retain only those timesteps for which corresponding radar observations were available. The final datasets grid is drawn in Fig. 4. Both datasets are available on Zenodo ([Stefanelli, 2025c](#)).

## 2.2. 3DVar formulation

In the 3DVar framework ([Lorenc, 1986](#)), the analysis state is obtained by minimising a cost function  $\mathcal{J}(\mathbf{x})$  that measures the distance of the model state  $\mathbf{x}$  to the background state  $\mathbf{x}_b$  and observations  $\mathbf{y}$ :

$$\mathcal{J}(\mathbf{x}) = \frac{1}{2}(\mathbf{x} - \mathbf{x}_b)^T \mathbf{B}^{-1} (\mathbf{x} - \mathbf{x}_b) + \frac{1}{2}(\mathbf{y} - \mathcal{H}(\mathbf{x}))^T \mathbf{R}^{-1} (\mathbf{y} - \mathcal{H}(\mathbf{x})) \quad (2)$$

Here,  $\mathbf{B}$  and  $\mathbf{R}$  denote the background and observation error covariance matrices, respectively, while  $\mathcal{H}$  is the non-linear observation operator that projects the model state into the observation space.

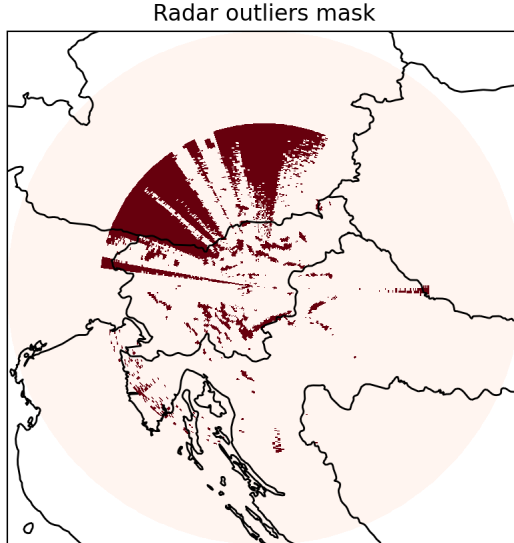


Figure 2: Spatial distribution of the global radar outlier mask derived from Mahalanobis-distance analysis of reflectivity data. The mask was computed only for data points within a 160 km radius of the Lisca radar that had already passed the initial filtering steps. Gates exceeding the 90th percentile distance threshold were classified as outliers (dark red) and excluded from subsequent use to enhance data quality.

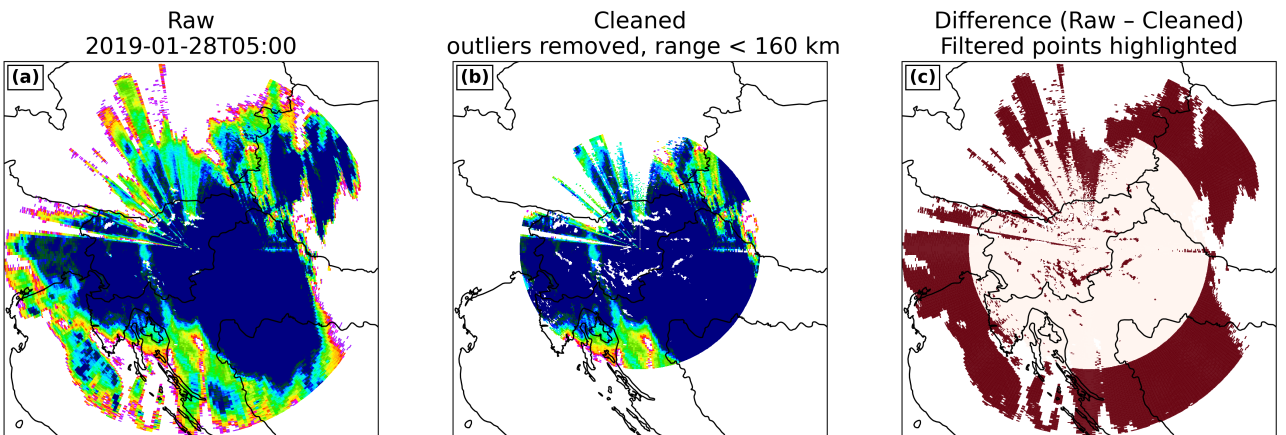


Figure 3: Example of the radar-data cleaning procedure. (a) raw reflectivity field showing radial artefacts, distant-range noise, and terrain-induced beam blockage effects. (b) cleaned field after applying the radial filtering, retaining only the observations in a disc of 160 km from the radar centre, and the Mahalanobis-distance outlier mask. (c) difference between the raw and cleaned fields, with filtered gates highlighted in dark red.

For observations that directly correspond to model variables, such as radiosonde-measured temperature or horizontal wind vector,  $\mathcal{H}$  typically consists only of interpolation and coordinate transformation procedures (Lahoz and Menard, 2010). However, when the observed quantity does not directly correspond to a model variable, as in the case of radar reflectivity, the construction of  $\mathcal{H}$  becomes considerably more complex. This is the case of the ALADIN 3DVar scheme for radar reflectivity data (Wattrelot et al., 2014), which retrieves pseudo-observations of relative humidity from observed vertical profiles of reflectivity using a one-dimensional Bayesian inversion. The resulting humidity pseudo-observations are subsequently assimilated in the AROME 3DVar system (Brousseau et al., 2011).

Minimising Eq. (2) requires computing its gradient, which vanishes at the minimum of the cost function:

$$\nabla \mathcal{J}(\mathbf{x}) = \mathbf{B}^{-1}(\mathbf{x} - \mathbf{x}_b) - \left( \frac{\partial \mathcal{H}(\mathbf{x})}{\partial \mathbf{x}} \right)^T \mathbf{R}^{-1}(\mathbf{y} - \mathcal{H}(\mathbf{x})). \quad (3)$$

The Jacobian of  $\mathcal{H}$ , i.e.  $\mathbf{H} = \partial \mathcal{H}(\mathbf{x}) / \partial \mathbf{x}$ , governs how observational information is backpropagated to the variables used to construct the observation operator during the minimisation.

For radar reflectivity, an accurate and differentiable observation operator is therefore essen-

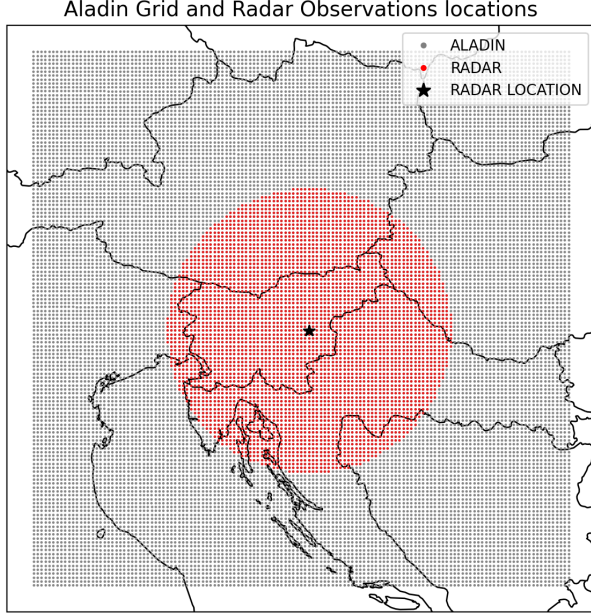


Figure 4: Spatial correspondence between the ALADIN model and radar datasets: black dots mark the model grid, and red dots denote radar observations interpolated onto the same spatial domain.

tial to ensure physically consistent increments and to enhance the quality of convective-scale analyses and forecasts.

In practice, the minimisation of Eq. (2) is performed in the incremental form (Courtier, 1997) and Eq. (2) reads as follows:

$$\mathcal{J}(\boldsymbol{\chi}) = \frac{1}{2} \boldsymbol{\chi}^\top \boldsymbol{\chi} + \frac{1}{2} (\mathbf{y} - \mathcal{H}(\mathbf{x}_b + \mathbf{L}\boldsymbol{\chi}))^\top \mathbf{R}^{-1} (\mathbf{y} - \mathcal{H}(\mathbf{x}_b + \mathbf{L}\boldsymbol{\chi})) \quad (4)$$

where  $\boldsymbol{\chi}$  is the control vector and  $\mathbf{L}$  the control variable transform (CVT) operator, such that

$$\delta\mathbf{x} = \mathbf{x} - \mathbf{x}_b = \mathbf{L}\boldsymbol{\chi} \quad (5)$$

In the defined control space,  $\mathbf{B}$  can be factorised as follows:

$$\mathbf{B} = \mathbf{L}\mathbf{L}^\top \quad (6)$$

In our implementation, we model the control operator  $\mathbf{L}$  as

$$\mathbf{L} = \mathbf{S}\mathbf{R}\mathbf{F} \quad (7)$$

where  $\mathbf{S}$  is a diagonal matrix containing the background-error variances of each model variable at each grid point and level, and  $\mathbf{RF}$  is the first-order recursive filter (RF) operator (Lorenz, 1992; Hayden and Purser, 1995; Purser et al., 2003) which defines the auto-covariance.

$\mathbf{S}$  is estimated from differences between forecasts and corresponding analyses valid at the same time, following a standard forecast–analysis statistics approach. For each season, we consider one representative month of ALADIN model output in 2019 (January, April, July and October for winter, spring, summer and autumn, respectively). For each month, 6 h lead-time forecast fields are paired with the corresponding analysis fields that are valid at the same synoptic times (00, 06, 12 and 18 UTC). Finally, for each variable  $q$  (t, u, v, r, t2m, r2m, msl) and the 4 pressure levels (975 hPa, 925 hPa, 850 hPa and 800 hPa) of 3-D variables, we compute the variance:

$$\mathbf{S} = \text{Var}[q^f - q^a] \quad (8)$$

where the superscripts  $f$  and  $a$  indicate forecast and analysis.

The RF is a simple iterative algorithm that requires only a few iterations to approximate the Gaussian function. The algorithm itself is 1-dimensional, but it can be straightforwardly applied in two or more dimensions by alternating dimensions between iterations (Purser et al., 2003). The RF methodology is used in oceanographic (Dobricic and Pinardi, 2008; Storto et al., 2021; Stefanelli et al., 2025) and atmospheric (Barker et al., 2004; Descombes et al., 2015) 3DVar applications.

We intentionally adopt this simple, univariate, flow-independent model of  $\mathbf{B}$ , with an isotropic RF in the horizontal, in order to keep the 3DVar configuration lightweight and robust as a proof-of-concept test case for the NN-based observation operator. All 3DVar experiments presented in the Section 3 use this specification of the control space and background-error covariance matrix with 4 RF iterations and a correlation radius of 10 km. We assumed the vertical autocovariances and cross-covariances to be zero.

In our experiments, the observation error covariance matrix  $\mathbf{R}$  is assumed diagonal (the observation errors are not correlated) with observation error standard deviation of 2 dBZ.

### 2.3. The NN-based observation operator

The nonlinear observation operator,  $\mathcal{H}$ , is implemented as a convolutional encoder–decoder NN that models the mapping from ALADIN model subspace to the radar reflectivity observation space. Formally, the operator approximates the transformation

$$\hat{\mathbf{y}} = D(E(\mathbf{x})) = \mathcal{H}(\mathbf{x}), \quad (9)$$

where  $D$  denotes the decoder and  $E$  the encoder.  $\mathbf{x}$  is the input vector of the neural network, which consists of the following ALADIN model fields: temperature ( $t$ ), horizontal wind components ( $u$ ) and ( $v$ ) and relative humidity ( $r$ ) at the first four pressure levels (975 hPa, 925 hPa, 850 hPa, and 800 hPa). In addition, 2 m temperature ( $t_{2m}$ ), 2 m relative humidity ( $r_{2m}$ ), and mean sea-level pressure ( $msl$ ) are provided to the network. These variables are chosen to capture the thermodynamic and dynamic conditions relevant to the precipitation formation. After the encoding-decoding process, the model-equivalent of the reflectivity field  $\hat{\mathbf{y}}$  is obtained. A schematic overview of the architecture is shown in Fig. 5.

The NN architecture is implemented as a residual U-Net (ResUNet, He et al., 2015). The ResUNet follows an encoder–decoder design with skip connections, residual blocks, and Squeeze-and-Excitation units (Hu et al., 2018) that apply channel-wise attention.

Training is guided by an edge-aware, spatially weighted loss. A Gaussian radial weight emphasises regions close to the radar, where observations are more reliable, while a boundary-enhancement map increases the loss along precipitation edges, where sharp reflectivity gradients occur. These weights modulate a composite loss combining Huber, gradient-difference, and Structural Similarity Index Measure (SSIM) terms, encouraging accurate amplitudes, sharp boundaries and structurally coherent patterns. For a detailed explanation of the ResUNet architecture and the implemented loss function, the reader is referred to Appendix A.

### 2.4. Training Setup

To learn the neural-network observation operator, we use analysis times (00, 06, 12, and 18 UTC) from 2019 to 2023, shuffled to avoid spurious correlations between consecutive timesteps. The first four years (2019–2022) are used for training and validation. The final year (2023) is held out as an independent test set and for 3DVar experiments.

Because precipitation events are comparatively rare in the training datasets, we apply targeted data augmentation to better represent reflectivity situations. Reflectivity events are defined as timesteps in which at least one grid point exceeds 13.5 dBZ. All such timesteps are extracted and augmented (Aggarwal et al., 2018) by rotating both the input ALADIN fields and the corresponding radar reflectivity by 90°, 180°, and 270° around the vertical axis. This procedure preserves the joint spatial structure of the model and radar fields while increasing the effective sample count for precipitation events.

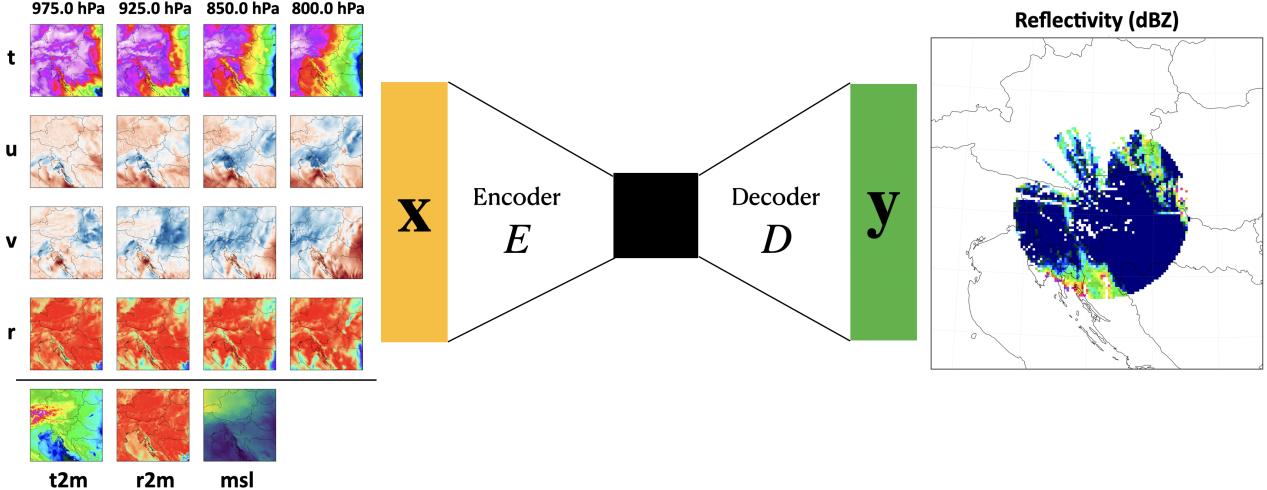


Figure 5: Schematic overview of the convolutional encoder–decoder neural network used to emulate the 3DVar observation operator. The model is trained with input  $\mathbf{x}$  consisting of ALADIN temperature ( $t$ ), relative humidity ( $r$ ), and horizontal wind components ( $u$  and  $v$ ) at four pressure levels (975 hPa, 925 hPa, 850 hPa, and 800 hPa), together with 2 m temperature ( $t_{2m}$ ), 2 m relative humidity ( $r_{2m}$ ), and mean sea-level pressure ( $msl$ ). The output  $\mathbf{y}$  is the reflectivity field measured by the radar, interpolated onto the model grid at the corresponding time.

The network is trained with a batch size of 16 using the Adam optimiser and an initial learning rate of  $10^{-3}$ . Training proceeds for a maximum of 1000 epochs, with early stopping applied if the validation loss does not improve for 10 consecutive epochs. In addition, an adaptive learning rate scheduler is employed. If the validation loss does not decrease for 3 epochs, the learning rate is reduced by a factor of 0.1 to improve convergence in the later stages of training (see [Appendix A](#) for further details). The model is implemented in PyTorch, and the code is available on Zenodo ([Stefanelli, 2025a](#)).

### 3. Results

The NN observation operator for radar reflectivities was first qualitatively assessed for different precipitation regimes ([Section 3.1](#)). To evaluate its performance beyond these illustrative examples, we next examine its behaviour in a range of data assimilation settings. In [Section 3.2](#), we analyse how assimilated radar observations induce analysis increments in the model variables through the gradient of the observation operator. For this purpose, we select a small subdomain of radar volumes (consisting of 250 observation points) to characterise the spatial structure, amplitude, and multivariate properties of the resulting increments. Finally, [Section 3.3](#) presents a Slovenian flood case study that documents the system’s performance during an extreme precipitation event and assesses whether the use of  $\mathcal{H}$  produces dynamically consistent analyses that better capture intense convective structures relevant to high-impact flooding. All the codes and  $\mathbf{B}$  matrices used are available on Zenodo ([Stefanelli, 2025b](#)).

#### 3.1. Performance in different precipitation regimes

To qualitatively assess how the NN-based observation operator behaves under different precipitation conditions, we inspected three cases with different characteristic precipitation regimes over the year 2023 (not used during the training of the operator): dry conditions ([Fig. 6 a,b](#)); broad stratiform precipitation ([Fig. 6 c,d](#)); complicated reflectivity patterns ([Fig. 6 e-h](#)). For each case, the observed radar reflectivity (used as target) is shown alongside the model-equivalent reflectivity field. The latter is obtained by applying the NN-based observation operator to the background state,  $\mathcal{H}(\mathbf{x}_b)$ .

Under dry conditions (2023-01-01T05:00, Fig. 6 a,b), both the observed reflectivity and its model equivalent  $\mathcal{H}(\mathbf{x}_b)$  are free of echoes. The NN operator correctly reproduces the absence of precipitation, indicating that it does not introduce spurious reflectivity under clear-sky conditions.

For broad stratiform precipitation (2023-08-05T00:00, Fig. 6 c,d), the operator captures the overall spatial extent of the radar echo and the large-scale reflectivity gradients. The main regions of moderate reflectivity are reasonably reproduced, although small-scale details differ between the two fields.

In cases with complicated reflectivity patterns (2023-01-09T06:00 and 2023-08-03T18:00, Fig. 6 e-h), associated with embedded convective elements and narrow bands, the network still reproduces the general spatial organisation of the echo, including the location and orientation of the main features. Nevertheless, differences appear in the fine-scale structure and local intensity, with some displacement and smoothing of individual convective cores. These examples illustrate that the NN-based operator performs consistently across regimes, from no-precipitation to complex convective situations.

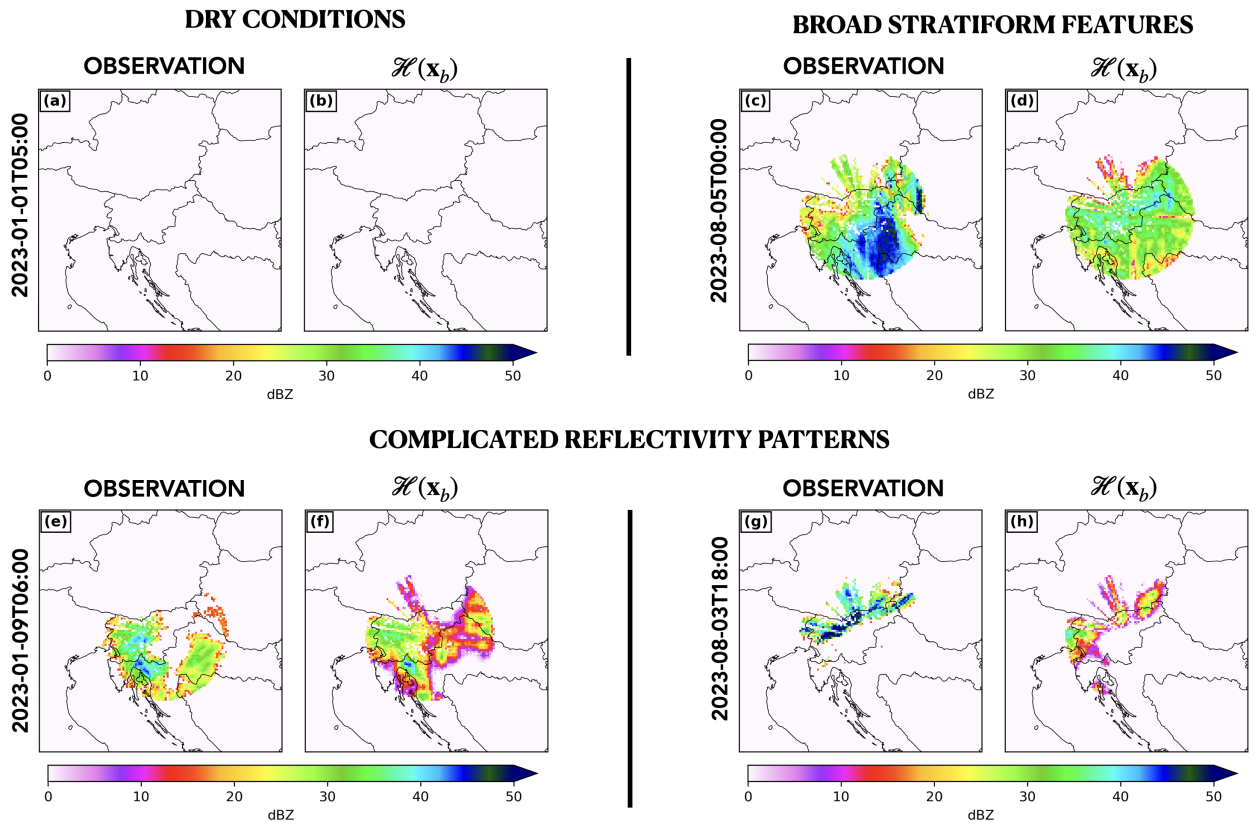


Figure 6: Generated versus observed radar reflectivity for four test samples. a, c, e, g show the radar reflectivity used as target observation and b, d, f, h the corresponding generated reflectivity field obtained from the background state,  $\mathcal{H}(\mathbf{x}_b)$ . a-b: dry conditions (no radar echo) on 2023-01-01T05:00. c-d: broad stratiform precipitation on 2023-08-05T00:00. e-h: two cases with complicated reflectivity patterns, including embedded convective structures on 2023-01-09T06:00 and 2023-08-03T18:00.

### 3.2. Increments in model state variables, induced by $\mathcal{H}$

To further investigate how the convolutional architecture of the NN-based observation operator spreads information in model space, we perform an idealised experiment in which a compact cluster of radar reflectivities is assimilated. The cluster consists of  $N = 250$  contiguous pixels (Fig. 7, small black disc).

To isolate the effect of  $\mathcal{H}$  itself, the background-error covariance matrix is set to the identity ( $\mathbf{B} = \mathbf{I}$ ), such that no spatial spreading arises from  $\mathbf{B}$ . Because the observation operator is defined to produce model-equivalent reflectivity values over the entire observed domain (see

Eq. 9), whereas  $\mathbf{y}$  represents only a subset of that domain, the cost function (2) is reformulated as

$$\mathcal{J}(\mathbf{x}) = \frac{1}{2}(\mathbf{x} - \mathbf{x}_b)^T(\mathbf{x} - \mathbf{x}_b) + \frac{1}{2}(\mathbf{y} - \mathbf{M}\mathcal{H}(\mathbf{x}))^T \mathbf{R}^{-1} (\mathbf{y} - \mathbf{M}\mathcal{H}(\mathbf{x})), \quad (10)$$

where  $\mathbf{M}$  is a masking matrix consisting of  $N$  row vectors, each containing zeros and a single element with a value of 1 representing the observed point.

A localisation mask is also defined within  $\nabla\mathcal{J}(\mathbf{x})$ . It is equal to 1 at all grid points inside the radar disc and 0 elsewhere (Fig. 7, large black disc). This mask ensures that only model variables at grid points within the disc can be updated during the cost function minimisation, while those outside remain fixed.

Fig. 7 displays the resulting analysis increments. The increments form a compact yet clearly multivariate structure aligned with the observation cluster and largely confined to the radar disc. Temperature and humidity show vertically coherent anomalies extending through the lower troposphere, while the wind increments exhibit dipole-like patterns. Some fields, most notably the near-surface temperature, exhibit weaker but non-negligible increments outside the immediate cluster.

Because  $\mathbf{B} = \mathbf{I}$  in this experiment, these patterns are entirely generated by the convolutional structure of  $\mathcal{H}$ . The results, therefore, demonstrate that, despite its CNN architecture, the NN-based observation operator produces increments that remain mainly localised around the assimilated reflectivity cluster, with limited extensions into the surrounding area, rather than inducing spurious long-range adjustments.

To assess how these model-space increments translate back into observation space, Fig. 8 compares the reflectivity observations with the background and analysis equivalents from the 250-pixel cluster experiment. The top row shows the observed reflectivity (Fig. 8-a), the model equivalent reflectivity from the model background state,  $\mathcal{H}(\mathbf{x}_b)$  (Fig. 8-b), and the model equivalent reflectivity from the analysis state,  $\mathcal{H}(\mathbf{x}_a)$  (Fig. 8-c). The background markedly underestimates the observed echo, producing a smoother and weaker pattern over the cluster disc. After assimilation (with  $\mathbf{B} = \mathbf{I}$ ), the analysis equivalent  $\mathcal{H}(\mathbf{x}_a)$  closely reproduces the observed reflectivity field, including the location and intensity of the main high-reflectivity cores.

The bottom row highlights the corresponding differences. Fig. 8-d shows the innovation  $\text{OBS} - \mathcal{H}(\mathbf{x}_b)$ , which is predominantly positive and large over the cluster disc, with a root-mean-square error (RMSE) of the observed region of 16.23 dBZ and 12.48 dBZ of the whole domain, reflecting the strong background underestimation. After assimilation, the residual  $\text{OBS} - \mathcal{H}(\mathbf{x}_a)$  (Fig. 8-e) in the observed region is reduced with an RMSE of 0.70 dBZ. The residual RMSE of the whole domain is 12.67 dBZ. The change in model-equivalent reflectivity,  $\mathcal{H}(\mathbf{x}_a) - \mathcal{H}(\mathbf{x}_b)$  is shown in Fig. 8-f. Together with the increment patterns in model space, this demonstrates that  $\mathcal{H}$  maps the local reflectivity cluster into a consistent multivariate response.

It is important to stress that, because  $\mathbf{B} = \mathbf{I}$  and no balance constraints are imposed, the resulting increments are not dynamically or thermodynamically consistent and should not be interpreted as a realistic atmospheric state. This experiment is purely diagnostic: it isolates the impact of the NN-based observation operator on the analysis and reveals its localisation and mapping properties, without any claim of physical realism in the resulting fields.

### 3.3. Slovenian floods case study

To illustrate the behaviour of the NN-based observation operator in a realistic high-impact weather event, we consider a case study on 4 August 2023 at 00UTC, characterised by widespread, intense precipitation over the radar domain that led to severe flooding and damage in Slovenia ([Agencija Republike Slovenije za Okolje \(ARSO\), 2023](#)). During this event, the 500 hPa geopotential field featured a warm ridge over southern Europe with an embedded trough over the Alps. This provided large-scale dynamical forcing with W-SW advection of moisture from the anomalously warm Mediterranean. The Dinaric-Alpine orography further enhanced convective development and rainfall intensity. The precipitation pattern was associated with a quasi-stationary triggering of convective cells (see Fig. 6g, showing observed reflectivity 6 h before

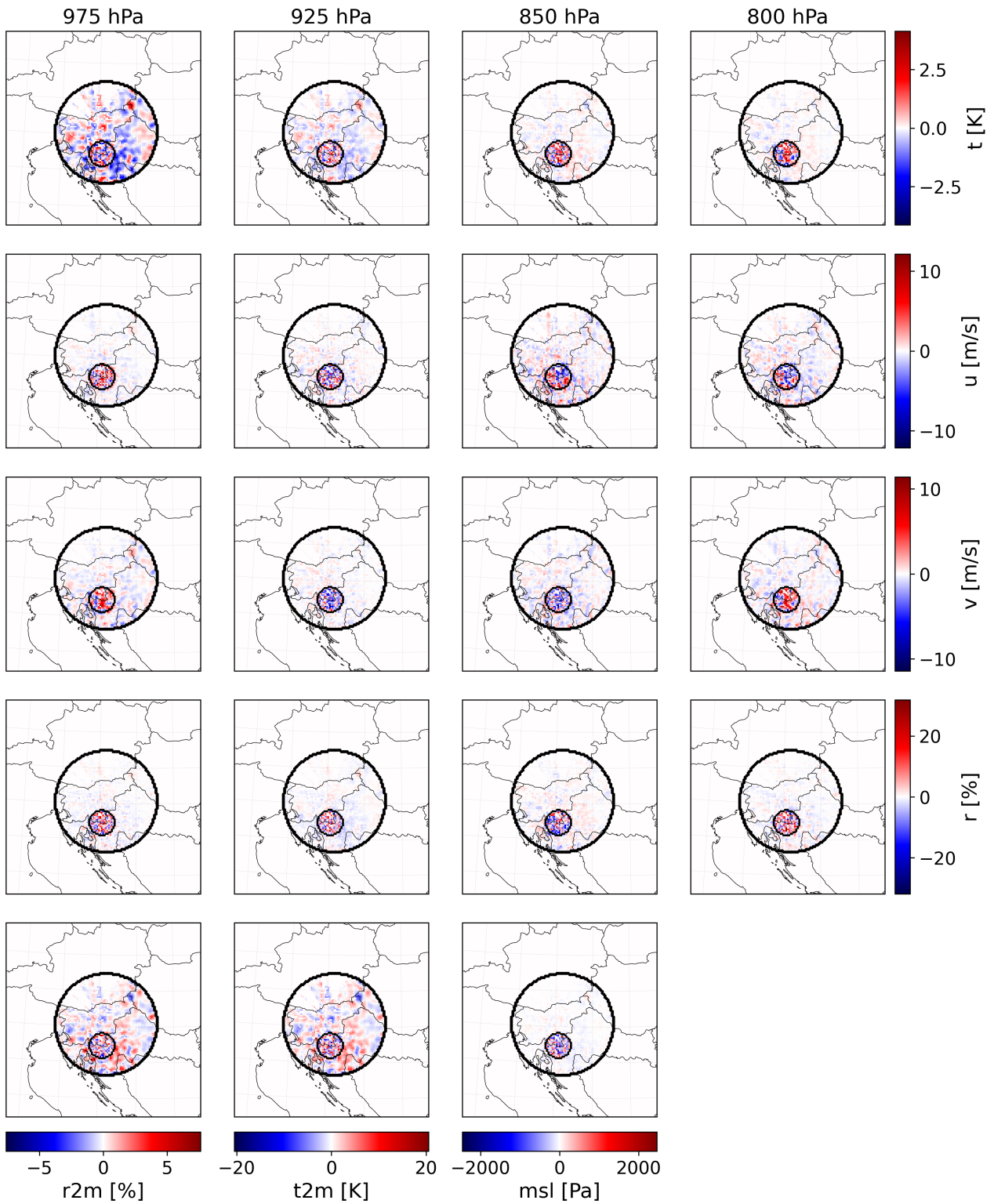


Figure 7: Analysis increments generated by the assimilation of a compact cluster of 250 reflectivity pixels and setting  $\mathbf{B} = \mathbf{I}$ . Columns show four pressure levels (975 hPa, 925 hPa, 850 hPa, and 800 hPa), while rows correspond to temperature  $t$ , zonal wind  $u$ , meridional wind  $v$ , relative humidity  $r$ , 2 m relative humidity ( $r2m$ ), 2 m temperature ( $t2m$ ), and mean sea-level pressure ( $msl$ ). The outer black circle denotes the radar disc and the inner circle the location of the assimilated cluster.

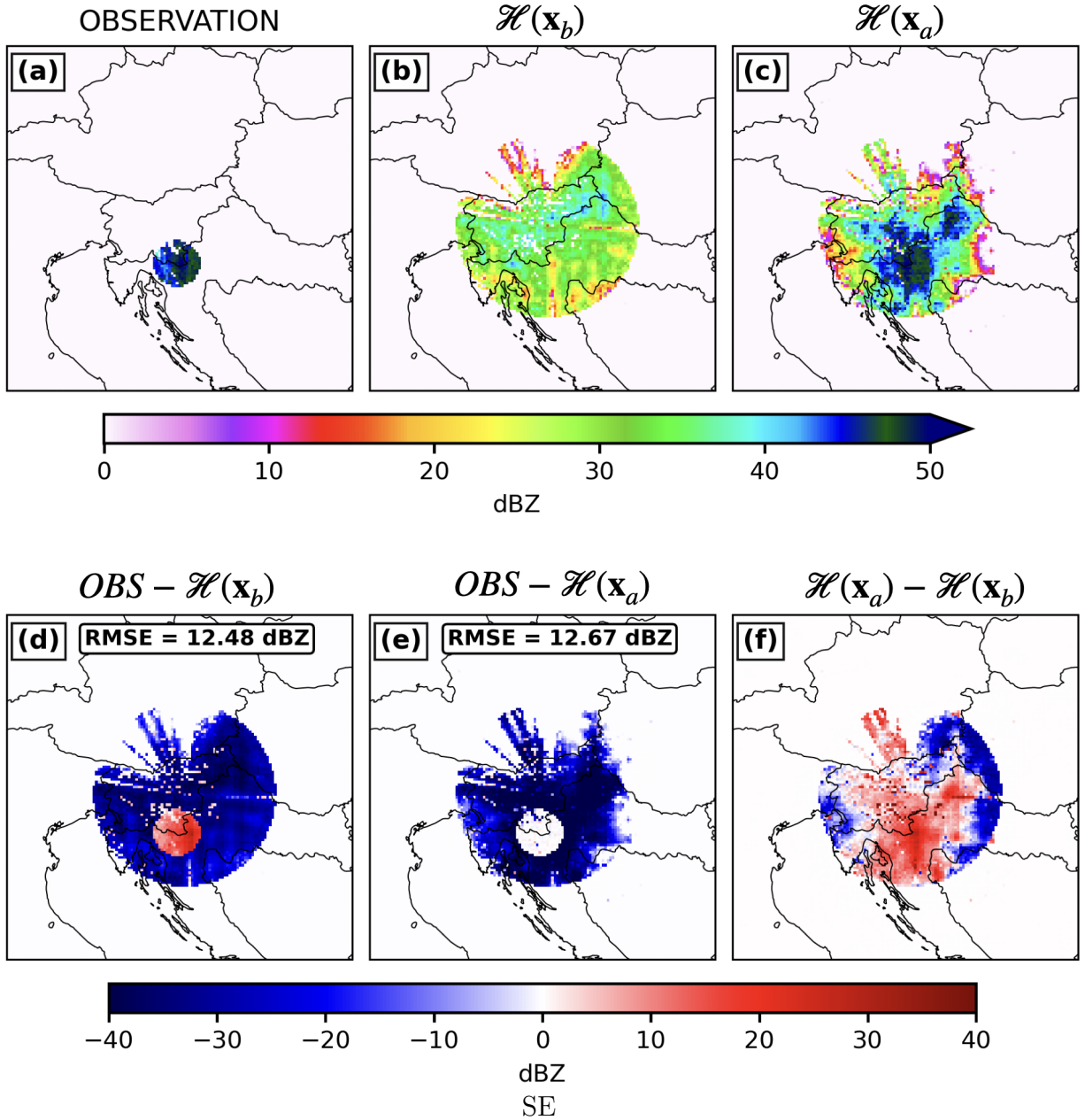


Figure 8: Evaluation of the NN-based observation operator for the experiment with a compact cluster of 250 assimilated pixels and  $\mathbf{B} = \mathbf{I}$ . Top row: (a) observed radar reflectivity, (b) background model-equivalent reflectivity  $\mathcal{H}(\mathbf{x}_b)$ , and (c) analysis model-equivalent reflectivity  $\mathcal{H}(\mathbf{x}_a)$ . Bottom row: (d) innovation  $\text{OBS} - \mathcal{H}(\mathbf{x}_b)$ . In the region of the observations location, RMSE = 16.23 dBZ (not shown) and RMSE = 12.48 dBZ for the whole domain, (e) residual  $\text{OBS} - \mathcal{H}(\mathbf{x}_a)$  with RMSE = 0.70 dBZ in the region of the observations location (not shown) and RMSE = 12.67 dBZ for the whole domain, and (f) change in model-equivalent reflectivity  $\mathcal{H}(\mathbf{x}_a) - \mathcal{H}(\mathbf{x}_b)$ .

the state analysed in Fig. 10a). As in Fig. 6g, Fig. 10a, shows the corresponding radar reflectivity field which exhibits a complex, elongated system with embedded convective elements and strong reflectivity gradients.

As in the previous section (Section 3.2), the localisation mask is defined as 1 over all grid points inside the radar disc and 0 elsewhere to ensure that the observation information is not spread with the gradient of  $\mathcal{H}$  outside the radar disc. Nevertheless, the  $\mathbf{B}$ -matrix spreads the impact of observations slightly across the disc boundary (Fig. 9). As a result, the analysis increment pattern reflects the combined action of the RF-based background autocovariances and the spatially extended, nonlinear mapping provided by NN-based  $\mathcal{H}$ . The properties of the applied  $\mathbf{B}$ -matrix are illustrated using a single observation experiment in [Appendix A.2](#).

The resulting multivariate increments are shown in Fig. 9. The increments exhibit a rich mesoscale structure, with alternating positive and negative anomalies of temperature, wind, humidity, mean sea level pressure, and 2 m variables that closely follow the organisation of the observed reflectivity system in Fig. 10a. Local dipoles and elongated features appear where strong reflectivity gradients are present, indicating that the NN-based observation operator is able to project information from the complex radar pattern onto dynamical and thermodynamical adjustments of the model state. At the same time, the increments remain confined to the radar disc and decay smoothly towards its edge, demonstrating that the combination of the localisation mask and the recursive-filter autocovariance successfully limits the spatial extent of the impact of the observations.

The impact of assimilating the full radar disc on the reflectivity field itself is summarised in Fig. 10. The top row shows: the observed reflectivity (Fig. 10a), the model equivalent reflectivity from the background  $\mathcal{H}(\mathbf{x}_b)$  (Fig. 10b) and the model equivalent reflectivity from the analysis  $\mathcal{H}(\mathbf{x}_a)$  (Fig. 10c). The analysis field clearly aligns more closely with the observation, particularly along the main high-reflectivity band and in the upstream convective cells.

The bottom panels display the innovation  $OBS - \mathcal{H}(\mathbf{x}_b)$  (Fig. 10d) and residual  $OBS - \mathcal{H}(\mathbf{x}_a)$  (Fig. 10e), together with their domain-averaged RMSE. Finally, Fig. 10f, shows  $\mathcal{H}(\mathbf{x}_a) - \mathcal{H}(\mathbf{x}_b)$ . Assimilation of the radar data reduces the RMSE from 5.99 dBZ to 3.47 dBZ, indicating a substantial improvement in the consistency between the model state and the observed reflectivity. Residual discrepancies are mainly confined to small-scale features and sharp gradients, which are only partially represented in the model fields and therefore cannot be fully corrected by the NN-based observation operator. Overall, the case study demonstrates that the proposed system can effectively pull the model state towards complex radar observations while preserving a physically reasonable multivariate increment structure.

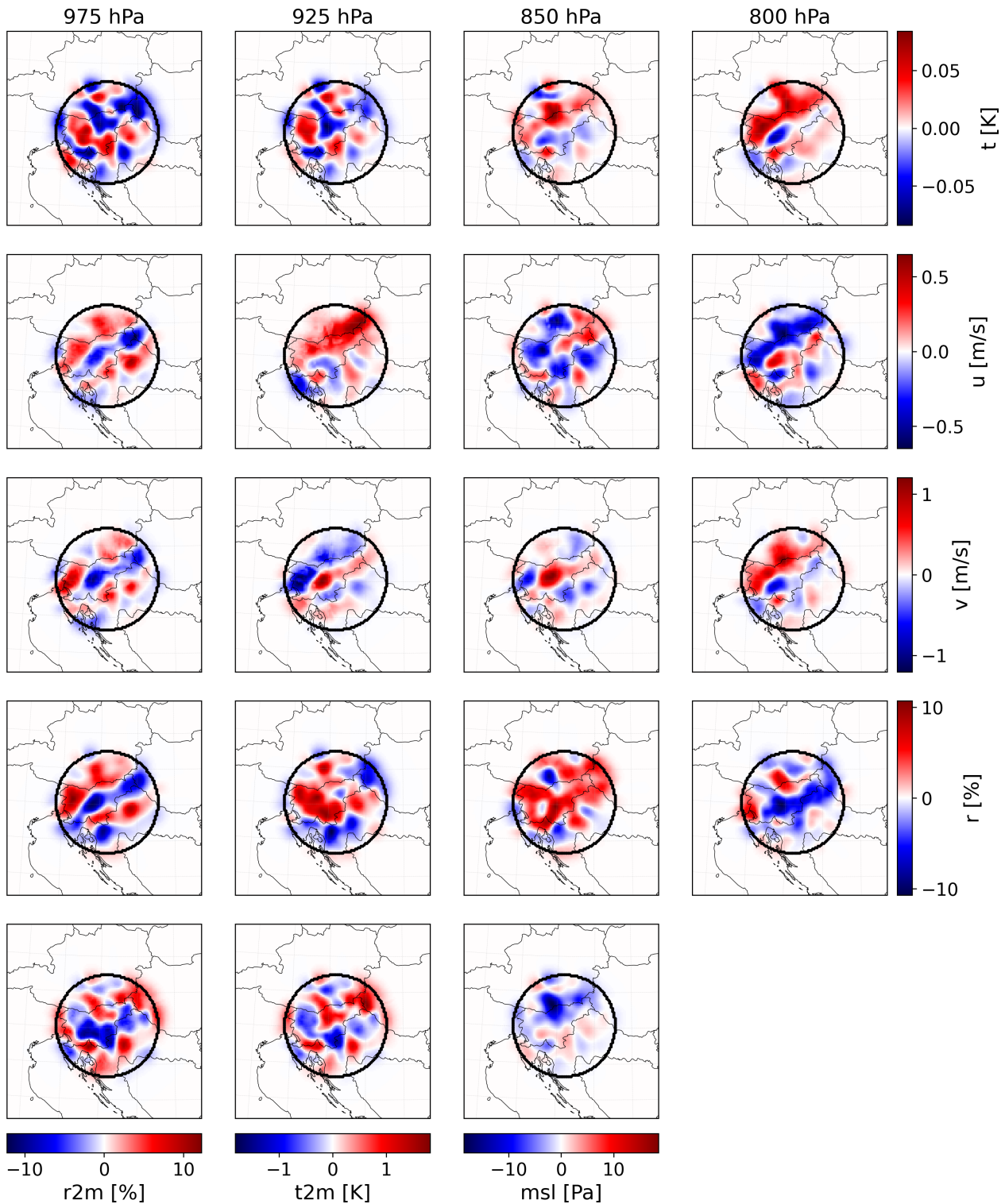


Figure 9: 3DVar analysis increments for the Slovenian floods case on 4 August 2023 at 00 UTC. Panels show increments of temperature ( $t$ ), meridional wind ( $v$ ), zonal wind ( $u$ ) and relative humidity ( $r$ ) at four pressure levels (975 hPa, 925 hPa, 850 hPa and 800 hPa), together with increments of 2-metre relative humidity ( $r_{2m}$ ), 2-metre temperature ( $t_{2m}$ ) and mean sea-level pressure (msl). The increments result from assimilating the full radar reflectivity field within the radar disc using the NN-based observation operator and the RF-based background-error covariance. The RF iterations are 4 and the correlation radius is 10 Km. The black circle denotes the radar disc and the inner circle the location of the assimilated cluster.

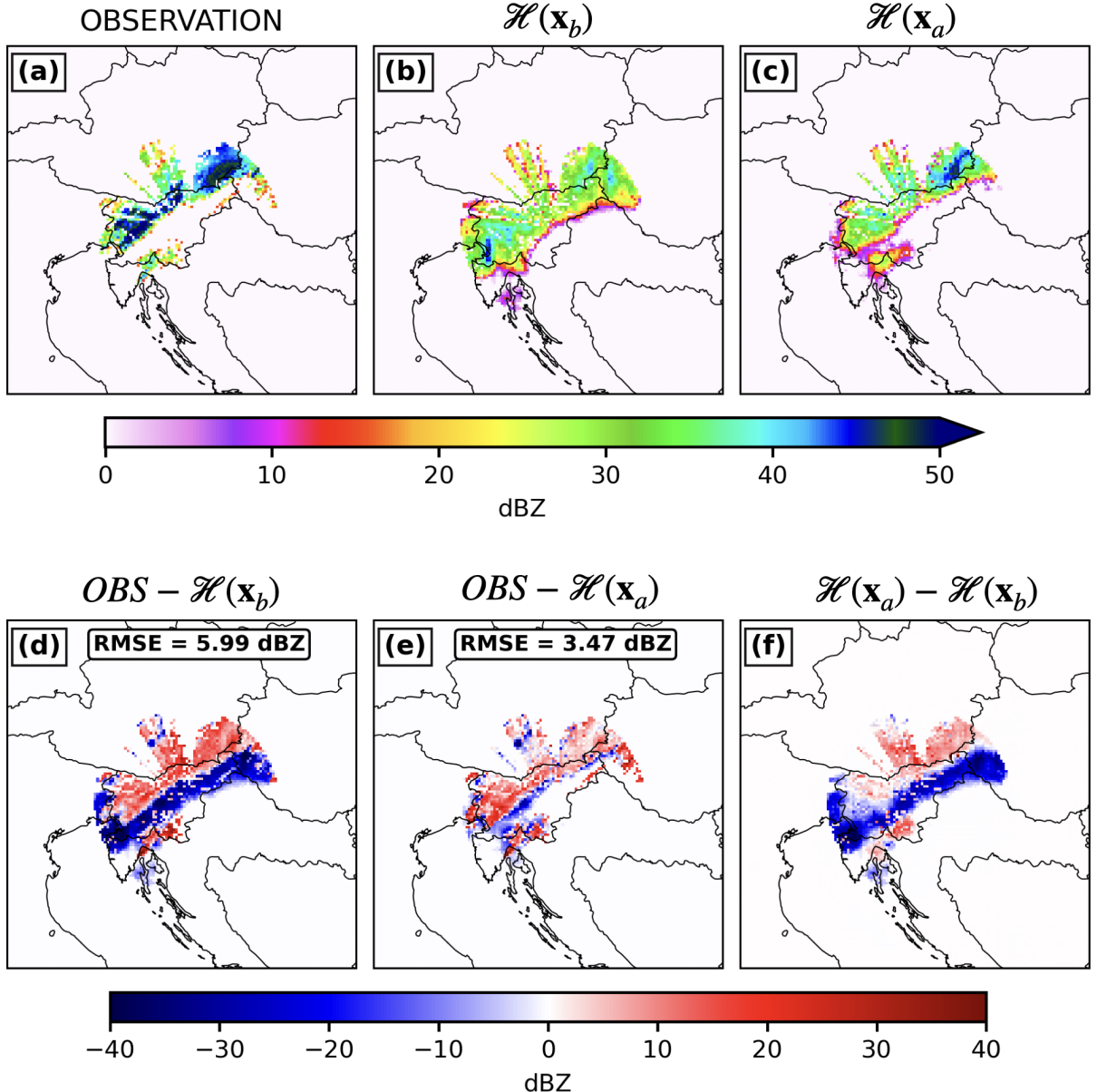


Figure 10: Evaluation of the NN-based observation operator for the Slovenian floods case on 4 August 2023 at 00 UTC. Top row: (a) observed radar reflectivity, (b) background model-equivalent reflectivity  $\mathcal{H}(\mathbf{x}_b)$ , and (c) analysis model-equivalent reflectivity  $\mathcal{H}(\mathbf{x}_a)$ . Bottom row: (d) innovation  $\text{OBS} - \mathcal{H}(\mathbf{x}_b)$  with RMSE = 5.99 dBZ, (e) residual  $\text{OBS} - \mathcal{H}(\mathbf{x}_a)$  with RMSE = 3.47 dBZ, and (f) change in model-equivalent reflectivity  $\mathcal{H}(\mathbf{x}_a) - \mathcal{H}(\mathbf{x}_b)$ .

## 4. Discussion and Conclusions

In this study, we have developed and tested a neural-network-based observation operator that maps short-range ALADIN model forecasts of temperature, humidity, horizontal wind components, and surface pressure to weather radar reflectivity within a 3DVar data assimilation framework. Using five years of radar and model data, we trained an encoder-decoder ResUNet to emulate the nonlinear relationship between model fields and observed reflectivities. We then embedded this operator into a 3DVar system with a simplified background-error covariance model to assess the behaviour of the operator in controlled experiments.

By learning a nonlinear mapping between model states and observations, this data-driven observation operator offers a flexible, differentiable alternative to traditional parameterised simulators of radar reflectivity. Our formulation allows, for the first time, to update dynamic and thermodynamic variables in the model state from the observed radar reflectivity data. The experiment assimilating a compact blob of 250 radar pixels (Section 3.2), the single observation experiment (Section [Appendix A.2](#)) and the August 2023 Slovenian floods case (Section 3.3) all show that radar reflectivity innovations are translated into analysis increments that modify humidity, temperature, wind, and surface pressure in a physically interpretable way, rather than merely adjusting the hydrometeor fields. The resulting analysis fields produce model-equivalent reflectivities that closely match the observed radar data.

A key property of the NN-based operator is that, because of its convolutional architecture, each simulated radar pixel is influenced by a broader neighbourhood of model state variables, allowing  $\mathcal{H}$  to exploit mesoscale patterns and gradients rather than purely local column information. However, most of the information is still gathered from the local proximity of the observation. As a consequence, its Jacobian spreads observational information along the horizontal structure of precipitation systems and increments align with the observed precipitation bands. In other words, the operator not only projects model variables into reflectivity space but also implicitly encodes cross-variable and cross-level relationships, as revealed by the single-observation and cluster experiments.

Despite these promising results, the present implementation has several limitations. First, we have not yet evaluated the impact of the NN-based operator on subsequent model forecasts. Because all experiments end at the analysis stage, no conclusions can yet be drawn regarding their effects on convective-scale prediction skill. Second, in this proof-of-concept configuration, hydrometeors were not included as input variables for training the NN operator to simulate radar reflectivity. In many operational radar DA systems, hydrometeors or precipitation-related variables can be directly updated through the DA, and the lack of such variables in our control vector limits the analysis's ability to directly adjust microphysical fields, even when reflectivity is well fitted. Third, the applied background-error covariance model is intentionally univariate:  $\mathbf{B}$  is built assuming diagonal variances and an isotropic recursive filter that represents only horizontal autocovariances. Vertical autocovariances and cross-covariances between different model variables are neglected.

Future work will therefore focus on addressing these limitations. A priority is to extend the control vector to include hydrometeor species and/or related microphysical variables, so that the NN-based operator can be used in combination with more physically explicit precipitation adjustments, as routinely done in operational systems. In parallel, we plan to replace the current univariate  $\mathbf{B}$  with a more realistic multivariate background-error covariance model that captures cross-variable and cross-scale balances, for example, by exploiting latent-space DA approaches based on autoencoders and unified neural covariance models (e.g. [Melinec and Zaplotnik, 2024](#) and [Melinec et al., 2025](#)). Finally, we aim to conduct full-cycle experiments using short-range forecasts in a regional domain, multiple radars, and additional case studies to quantify the impact of this framework on thunderstorm predictability.

More broadly, our results illustrate both the potential and the difficulties of integrating machine learning into geophysical DA systems. On the positive side, NN-based observation operators can capture complex, nonlinear relationships that are difficult to express analyti-

cally, while remaining fully differentiable and thus compatible with variational methods. We hope that the methodology and open datasets presented here will help the DA community to more systematically evaluate NN-based observation operators, encourage transparent diagnostic practices, and accelerate the transition from proof-of-concept prototypes to robust, operationally relevant systems.

## Funding

This publication is supported by the European Union’s Horizon Europe research and innovation program under the Marie Skłodowska-Curie COFUND Postdoctoral Programme, SMASH co-funded under the grant agreement No.101081355 and by the Republic of Slovenia and the European Union from the European Regional Development Fund.

This research was supported by the Slovenian Research And Innovation Agency (Javna agencija za znanstvenoraziskovalno in inovacijsko dejavnost RS) research core funding No. P1-0188. This research was further supported by the University of Ljubljana Grant SN-ZRD/22-27/0510. Žiga Zaplotnik acknowledges the funding by the European Union under the Destination Earth initiative and Copernicus Climate Change Service (C3S).

## Author Contributions

M.S. - Data curation, Formal analysis, Software, Validation, Visualisation, Writing (original draft preparation), Conceptualisation, Methodology, Investigation, Funding acquisition, Project administration, Writing (review and editing), Ž.Z. - Conceptualisation, Methodology, Investigation, Funding acquisition, Project administration, Writing (review and editing), G.S. - Investigation, Funding acquisition, Project administration, Writing (review and editing).

## Acknowledgements

MS thanks the Theoretical and Scientific Data Science group at SISSA for hospitality during the first secondment. In particular, Roberto Trotta and Serafina Di Gioia for their valuable discussions and suggestions. MS also thanks the Slovenian Met Office (ARSO) for hospitality during the second secondment and for providing the ALADIN model and radar data used in this study. In particular, Benedikt Strajnar, Jure Cedilnik, and Neva Pristov for valuable discussions and suggestions. Finally, MS thanks Uroš Perkan for valuable discussions and suggestions.

## Code and data availability

All codes used in this study are written in Python and, together with the datasets, are publicly archived on Zenodo under the Creative Commons Attribution 4.0 International (CC BY 4.0) license.

The nonlinear neural-network-based observation operator used to map ALADIN numerical weather prediction model outputs to radar-reflectivity observation space is available as the repository “3DVar Neural Network-Based Observation Operator” ([Stefanelli, 2025a](#)). The directory structure includes a TEST subdirectory containing a ready-to-use trained ResUNet model. The dataset necessary to train the model is “LISCA-ALADIN HNN” ([Stefanelli, 2025c](#)).

The 3DVar data assimilation system is also archived on Zenodo as the repository “3DVar for Neural Network-Based Observation Operator” ([Stefanelli, 2025b](#)). It contains the 3DVar configurations used in this study and auxiliary datasets (precomputed **B**-matrix and the observation-space mask) needed to run and test the system.

## Conflict of Interest Statement

The authors declare no conflicts of interest.

## **Disclaimer**

Co-funded by the European Union. Views and opinions expressed are, however, those of the author(s) only and do not necessarily reflect those of the European Union or European Research Executive Agency. Neither the European Union nor the granting authority can be held responsible for them.

## Bibliography

Agencija Republike Slovenije za Okolje (ARSO): Izjemne poplave v Sloveniji med 4. in 8. avgustom 2023, Tech. rep., Urad za meteorologijo, hidrologijo in oceanografijo, Agencija Republike Slovenije za okolje, Ljubljana, Slovenia, URL [http://hmljn.ars.si/vode/poro%C4%8Dila%20in%20publikacije/Porocilo\\_visoke\\_vode\\_in\\_poplave\\_avg2023.pdf](http://hmljn.ars.si/vode/poro%C4%8Dila%20in%20publikacije/Porocilo_visoke_vode_in_poplave_avg2023.pdf), in Slovenian, 2023.

Aggarwal, C. C. et al.: Neural networks and deep learning, vol. 10, Springer, 2018.

Barker, D. M., Huang, W., Guo, Y.-R., Bourgeois, A., and Xiao, Q.: A three-dimensional variational data assimilation system for MM5: Implementation and initial results, *Monthly Weather Review*, 132, 897–914, 2004.

Brousseau, P., Berre, L., Bouttier, F., and Desroziers, G.: Background-error covariances for a convective-scale data-assimilation system: AROME-France 3D-Var, *Quarterly Journal of the Royal Meteorological Society*, 137, 409–422, 2011.

Cheng, S., Quilodrán-Casas, C., Ouala, S., Farchi, A., Liu, C., Tandeo, P., Fablet, R., Lucor, D., Iooss, B., Brajard, J., et al.: Machine learning with data assimilation and uncertainty quantification for dynamical systems: a review, *IEEE/CAA Journal of Automatica Sinica*, 10, 1361–1387, 2023.

Courtier, P.: Variational methods (gtSpecial IssueltData assimilation in meteorology and oceanography: theory and practice), *Journal of the Meteorological Society of Japan. Ser. II*, 75, 211–218, 1997.

Descombes, G., Auligné, T., Vandenberghe, F., Barker, D., and Barre, J.: Generalized background error covariance matrix model (GEN\_BE v2. 0), *Geoscientific Model Development*, 8, 669–696, 2015.

Dobricic, S. and Pinardi, N.: An oceanographic three-dimensional variational data assimilation scheme, *Ocean modelling*, 22, 89–105, 2008.

Doviak, R. J. and Zrnic, D. S.: Doppler radar & weather observations, Academic press, 2014.

Dowell, D. C., Wicker, L. J., and Snyder, C.: Ensemble Kalman filter assimilation of radar observations of the 8 May 2003 Oklahoma City supercell: Influences of reflectivity observations on storm-scale analyses, *Monthly Weather Review*, 139, 272–294, 2011.

Fabry, F. and Meunier, V.: Why are radar data so difficult to assimilate skillfully?, *Monthly Weather Review*, 148, 2819–2836, 2020.

Franch, G., Maggio, V., Covello, L., Pendesini, M., Jurman, G., and Furlanello, C.: TAAS-RAD19, a high-resolution weather radar reflectivity dataset for precipitation nowcasting, *Scientific Data*, 7, 234, 2020.

Grover, M., Mühlbauer, K., Goudensoofdt, E., Syed, H. A., Ladino, A., Jackson, R., and Wolfensberger, D.: openradar/xradar: xradar v0.10.0, doi:10.5281/zenodo.15862221, URL <https://doi.org/10.5281/zenodo.15862221>, 2025.

Hayden, C. M. and Purser, R. J.: Recursive filter objective analysis of meteorological fields: Applications to NESDIS operational processing, *Journal of Applied Meteorology and Climatology*, 34, 3–15, 1995.

He, K., Zhang, X., Ren, S., and Sun, J.: Deep residual learning, *Image Recognition*, 7, 327–336, 2015.

Hu, J., Shen, L., and Sun, G.: Squeeze-and-excitation networks, in: Proceedings of the IEEE conference on computer vision and pattern recognition, pp. 7132–7141, 2018.

Lahoz, B. K. W. and Menard, R.: Data assimilation, Springer, 2010.

Liu, C., Xue, M., and Kong, R.: Direct variational assimilation of radar reflectivity and radial velocity data: Issues with nonlinear reflectivity operator and solutions, *Monthly Weather Review*, 148, 1483–1502, 2020.

Lorenc, A.: Iterative analysis using covariance functions and filters, *Quarterly Journal of the Royal Meteorological Society*, 118, 569–591, 1992.

Lorenc, A. C.: Analysis methods for numerical weather prediction, *Quarterly Journal of the Royal Meteorological Society*, 112, 1177–1194, 1986.

Melinc, B. and Zaplotnik, Ž.: 3D-Var data assimilation using a variational autoencoder, *Quarterly Journal of the Royal Meteorological Society*, 150, 2273–2295, 2024.

Melinc, B., Perkan, U., and Zaplotnik, Ž.: A unified neural background-error covariance model for midlatitude and tropical atmospheric data assimilation, arXiv preprint arXiv:2506.11968, 2025.

Pasmans, I., Chen, Y., Sebastian Finn, T., Bocquet, M., and Carrassi, A.: Ensemble Kalman filter in latent space using a variational autoencoder pair, *Quarterly Journal of the Royal Meteorological Society*, p. e70070, 2025.

Purser, R. J., Wu, W.-S., Parrish, D. F., and Roberts, N. M.: Numerical aspects of the application of recursive filters to variational statistical analysis. Part I: Spatially homogeneous and isotropic Gaussian covariances, *Monthly Weather Review*, 131, 1524–1535, 2003.

Sebastianelli, S., Russo, F., Napolitano, F., and Baldini, L.: On precipitation measurements collected by a weather radar and a rain gauge network, *Natural Hazards and Earth System Sciences*, 13, 605–623, 2013.

Stefanelli, M.: 3DVar Neural Network-Based Observation Operator, doi:10.5281/zenodo.17898084, URL <https://doi.org/10.5281/zenodo.17898084>, 2025a.

Stefanelli, M.: 3DVar for Neural Network-Based Observation Operator, doi:10.5281/zenodo.17899025, URL <https://doi.org/10.5281/zenodo.17899025>, 2025b.

Stefanelli, M.: LISCA-ALADIN HNN, doi:10.5281/zenodo.17880622, URL <https://doi.org/10.5281/zenodo.17880622>, 2025c.

Stefanelli, M., Jansen, E., Aydogdu, A., Federico, I., and Coppini, G.: Data assimilation for advanced cross-scale unstructured grid ocean modelling, *Frontiers in Marine Science*, 12, 1656879, doi:10.3389/fmars.2025.1656879, URL <https://doi.org/10.3389/fmars.2025.1656879>, 2025.

Stephan, K., Klink, S., and Schraff, C.: Assimilation of radar-derived rain rates into the convective-scale model COSMO-DE at DWD, *QJ Roy. Meteor. Soc.*, 134, 1315–1326, 2008.

Storto, A., De Magistris, G., Falchetti, S., and Oddo, P.: A neural network-based observation operator for coupled ocean–acoustic variational data assimilation, *Monthly Weather Review*, 149, 1967–1985, 2021.

Stržinar, G. and Skok, G.: Comparison and optimization of radar-based hail detection algorithms in Slovenia, *Atmospheric Research*, 203, 275–285, doi:10.1016/j.atmosres.2018.01.005, 2018.

Termonia, P., Fischer, C., Bazile, E., Bouyssel, F., Brožková, R., Bénard, P., Bochenek, B., Degrauwe, D., Derková, M., Khatib, R. E., Hamdi, R., Mašek, J., Pottier, P., Přistov, N., Seity, Y., Smolíková, P., Španiel, O., Tudor, M., Wang, Y., Wittmann, C., and Joly, A.: The ALADIN System and its canonical model configurations AROME CY41T1 and ALARO CY40T1, Geoscientific Model Development, 11, 257–281, doi:10.5194/gmd-11-257-2018, 2018.

Thiruvengadam, P. and Ghosh, S.: Radar reflectivity and radial velocity assimilation in a hybrid ETKF-3DVAR system for prediction of a heavy convective rainfall, Quarterly Journal of the Royal Meteorological Society, 147, 2264–2280, 2021.

Wattrelot, E., Caumont, O., and Mahfouf, J.-F.: Operational implementation of the 1D+ 3D-Var assimilation method of radar reflectivity data in the AROME model, Monthly Weather Review, 142, 1852–1873, 2014.

World Meteorological Organization (Lisca wgs84): Lisca wgs84, URL <https://wrd.mgm.gov.tr/Radar/Details/VlczcSt1TG1XZHh3NWdyclUrZmo4QT09>, 2025.

## Appendices

### Appendix A. Neural Network Architecture

The observation operator  $\mathcal{H}$  is estimated using a residual U-Net (ResUNet, He et al., 2015) to map multi-level meteorological model fields to radar reflectivity observations at the same spatial resolution. The input tensor  $\mathbf{x} \in \mathbb{R}^{B \times 19 \times H \times W}$  comprises 19 channels of model fields: four pressure levels (975 hPa, 925 hPa, 850 hPa and 800 hPa) of temperature ( $t$ ), zonal wind ( $u$ ), meridional wind ( $v$ ), and relative humidity ( $r$ ), comprising 16 channels, together with three surface variables: 2 m temperature ( $t2m$ ), 2 m relative humidity ( $r2m$ ) and mean sea-level pressure ( $msl$ ). The model outputs a single-channel radar field  $\hat{\mathbf{y}} \in \mathbb{R}^{B \times 1 \times H \times W}$ . The input and output fields share the same spatial dimensions, both having  $H = W = 137$ .

The architecture follows an encoder-decoder topology with symmetric skip connections between corresponding resolutions. Each encoder (**E**) stage consists of a residual block:

$$\begin{aligned} \mathbf{E}_1 &= R_1(\mathbf{x}) \\ \mathbf{E}_i &= R_i(\text{MP}_2(\mathbf{E}_{i-1})), \quad i = 2, 3, 4 \end{aligned} \tag{A.1}$$

where  $\text{MP}_2$  denotes  $2 \times 2$  max pooling, and  $R_i$  represents a residual block composed of two  $3 \times 3$  convolutions with Batch Normalisation and LeakyReLU activations, plus a skip connection with projection when the number of channels changes. Within each block, a Squeeze-and-Excitation (SE) unit (Hu et al., 2018) performs channel-wise attention by scaling feature maps according to a learned relevance weight derived from global average pooling. The encoder feature dimensions are  $\{16, 32, 64, 128\}$ .

The decoder (**D**) performs progressive upsampling via transposed convolutions and skip concatenations:

$$\mathbf{D}_j = R_j(\text{TC}_2(\mathbf{E}_j) \oplus C(\mathbf{E}_{j-1})) \quad j = 4, 3, 2 \tag{A.2}$$

where  $\text{TC}_2$  denotes a  $2 \times 2$  transposed convolution with stride 2,  $C(\cdot)$  is a center-cropping operator ensuring spatial alignment and the symbol  $\oplus$  represents concatenation along the channel dimension. The decoder feature dimensions are  $\{64, 32, 16\}$ . A final  $1 \times 1$  convolution layer projects the decoder output to one channel:

$$\hat{\mathbf{y}} = \text{Conv}_{1 \times 1}(\mathbf{D}_2) \tag{A.3}$$

where  $\hat{\mathbf{y}}$  is the model equivalent reflectivity. To preserve grid consistency, all outputs are adjusted using symmetric reflect padding and cropping operations so that  $\text{size}(\hat{\mathbf{y}}) = (H, W)$ , even for odd input dimensions (e.g.,  $137 \times 137$ ).

The ResUNet thus combines multiscale feature extraction, residual learning, and channel attention in a compact architecture that effectively translates numerical weather prediction (NWP) predictor fields into spatially coherent radar observations.

### Appendix A.1. Loss Function

To guide the model toward physically meaningful learning, we introduce a spatially and structurally aware loss weighting strategy. The objective is not to alter the definition of the loss terms themselves, but to control the spatial distribution of their influence during training.

#### Appendix A.1.1. Gaussian Spatial Weighting Based on Radar Coverage

To reflect the varying reliability of radar observations with distance from the radar location (Sebastianelli et al., 2013), we define a spatial weighting field that decays smoothly as a Gaussian function.

After preprocessing, the radar and model share the same spatial grid, but valid observations are confined to a circular domain of a radius of 160 km (Fig. 4). Since measurement uncertainty and beam broadening increase with distance, pixels farther from the radar are assigned lower weights in the loss computation.

The weighting map is first initialised by identifying the spatial extent of valid reflectivity data, producing a binary mask of observed regions, which is then combined with a Gaussian decay computed from the Euclidean distance,  $d(x, y)$ , to the radar centre. The Gaussian profile is defined as

$$W_g(x, y) = \begin{cases} w_{g_{\text{inner}}}, & \text{if } d(x, y) < r_{\text{inner}} \\ \exp\left(-\frac{d(x, y)^2}{2\sigma^2}\right), & \text{otherwise} \end{cases} \quad (\text{A.4})$$

For this study, we used  $\sigma = 45$  km to control the rate of decay. Within a central radius of  $r_{\text{inner}} = 20$  km, the weights are kept constant ( $w_{g_{\text{inner}}} = 0.9$ ) to avoid overemphasising a very small core region, ensuring a smooth transition from the inner plateau to the decaying outer field. The inner plateau ensures uniform weighting near the centre, while the Gaussian tail gradually downweights peripheral regions.

This spatial weighting acts as a physically informed prior: errors near the radar, where observations are most accurate, contribute more strongly to the loss, while those in peripheral regions, where measurement uncertainty is higher, are gradually downweighted. The resulting Gaussian weight field is shown in Fig. A.11, illustrating the smooth radial decay centred at the radar position.

#### Appendix A.1.2. Boundary-Enhanced Target Weighting

Radar reflectivity fields often exhibit sharp gradients at storm boundaries. In this context, “storm boundaries” refer to boundaries in the radar-observed reflectivity field, which do not always coincide with the true physical extent of the storm. In particular, for shallow systems (e.g. during the cold season or at long ranges), the radar beam may overshoot hydrometeors, so that the apparent echo edge in reflectivity is displaced relative to the actual precipitation boundary. Consequently, we introduce a boundary-emphasis map  $W_b$  derived from the ground-truth field to preserve such discontinuities.  $W_b$  emphasises transitions in the observation space defined by the radar product, rather than enforcing strict physical storm edges. This mechanism is designed to assign higher importance to pixels located along the transition between precipitating and non-precipitating regions, where small spatial displacements may produce substantial structural errors. Following, we discuss the methodology used to construct  $W_b$ .

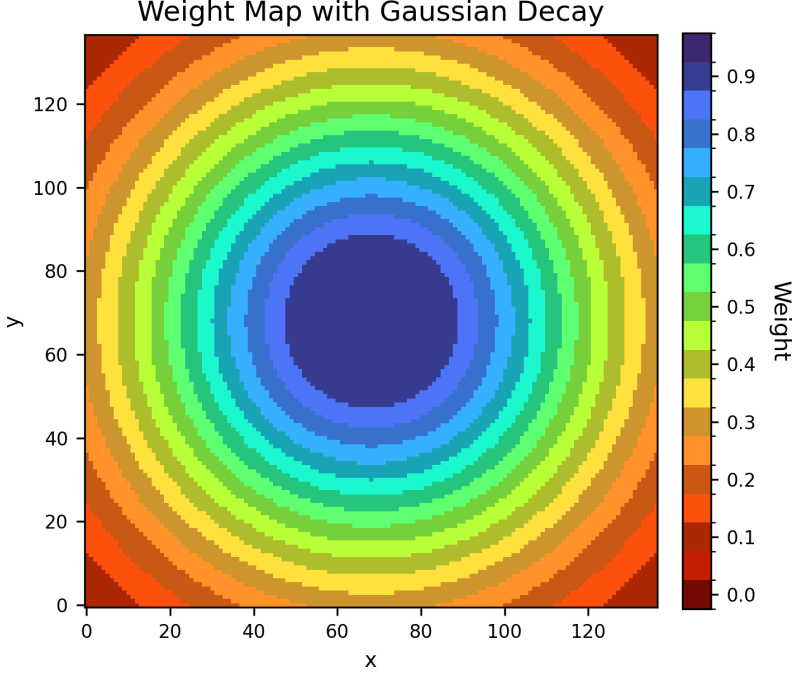


Figure A.11: Spatial weighting map used in the loss function. The weights follow a Gaussian decay centred at the radar location, with higher importance near the radar and reduced weights farther away.

*Binary mask construction.* During the training, the NaN reflectivity values are set to 0. Let  $T \in \mathbb{R}^{H \times W}$  denote the target reflectivity field. We first construct a binary mask

$$M(x, y) = \begin{cases} 1, & T(x, y) > 0 \\ 0, & T(x, y) = 0 \end{cases} \quad (\text{A.5})$$

which identifies the support of non-zero reflectivity.

*Morphological dilation and erosion.* To extract the boundary of the support region, we apply dilation,  $\text{Dil}(\cdot)$ , and erosion,  $\text{Ero}(\cdot)$ , using a square structuring element of width  $2r + 1$ , where  $r$  is the user-specified boundary radius in pixels (3 in this study). In the implementation, both operations are performed using two-dimensional max-pooling layers:

$$\text{Dil}(M) = \text{maxpool}(M; 2r + 1, \text{stride} = \text{padding} = r) \quad (\text{A.6})$$

$$\text{Ero}(M) = 1 - \text{maxpool}(1 - M; 2r + 1, \text{stride} = 1, \text{padding} = r) \quad (\text{A.7})$$

The dilation operation expands the support region outward by  $r$  pixels, whereas erosion shrinks it inward by the same amount. Their difference characterizes the thin ring enclosing the original boundary.

*Boundary-ring extraction.* The raw boundary mask is obtained as

$$R = \max(\text{Dil}(M) - \text{Ero}(M), 0) \quad (\text{A.8})$$

which yields a binary ring of approximate thickness  $2r$  surrounding the transition zone between zero and nonzero reflectivity. Pixels in this ring correspond to locations where edge fidelity is most relevant for visual and physical accuracy.

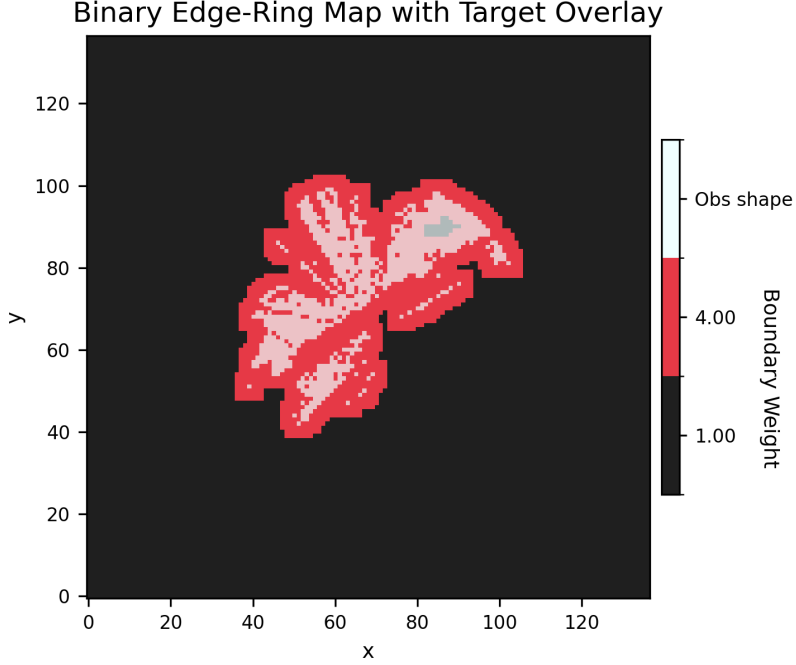


Figure A.12: Boundary-enhancement weighting map with overlaid observation footprint. Red pixels indicate the boundary-weighting ring produced by the dilation–erosion operation, where the loss is locally amplified to emphasise sharp reflectivity transitions. Black pixels represent regions where no additional weighting is applied. The light-blue overlay corresponds to the target observation region, illustrating the spatial extent of valid radar reflectivity data. Together, these fields show how the boundary-weighting mechanism selectively increases the loss contribution only along the edges of the observed precipitation structures.

*Weight assignment.* The final boundary-enhanced weight map is defined as

$$W_b(x, y) = 1 + \beta R(x, y) \quad (\text{A.9})$$

where  $\beta > 0$  is a tunable amplification factor (3 in this study). Pixels in the boundary ring thus receive a weight of  $1 + \beta$ , while all other pixels retain unit weight. In practice,  $\beta$  values in the range 2–4 provide a moderate emphasis without destabilising optimisation. An example of boundary weights is shown in Fig. A.12.

*Effect on training.* This boundary emphasis increases the penalty for structural errors near storm edges, helping to preserve sharp gradients, improve spatial coherence, and reduce the tendency of neural networks to oversmooth precipitation boundaries. The method is computationally inexpensive, differentiable with respect to predictions, and compatible with any pixelwise loss formulation.

#### Appendix A.1.3. Combined Spatial Weight Map

The total spatial weighting applied during training is obtained by the normalized product

$$W(x, y) = \frac{W_g(x, y) W_b(x, y)}{\overline{W_g} \overline{W_b}} \quad (\text{A.10})$$

where the denominator denotes the mean over all spatial elements. Normalization maintains a unit mean weight, thereby stabilizing the overall gradient magnitude and learning rate.

#### Appendix A.1.4. Edge-Aware Weighted Loss

Given a model prediction  $P$  and corresponding target field  $T$ , the network is trained using the following composite loss function

$$\mathcal{L} = \lambda_{\text{Huber}} \mathcal{L}_{\text{Huber}} + \lambda_{\text{grad}} \mathcal{L}_{\text{grad}} + \lambda_{\text{SSIM}} \mathcal{L}_{\text{SSIM}} \quad (\text{A.11})$$

where all pixelwise components are modulated by a shared spatially varying weight map  $W$ . The first term, the Huber loss,

$$\mathcal{L}_{\text{Huber}} = \frac{1}{N} \sum_{x,y} W(x,y) h(P(x,y) - T(x,y)) \quad (\text{A.12})$$

uses the Huber function  $h(\cdot)$

$$h(x) = \begin{cases} \frac{1}{2}x^2/\delta, & |x| \leq \delta \\ |x| - \frac{\delta}{2}, & |x| > \delta \end{cases} \quad (\text{A.13})$$

and provides robustness to outliers while preserving sensitivity to small errors.

Edge preservation is encouraged through the gradient-difference term

$$\mathcal{L}_{\text{grad}} = \frac{1}{N} \sum_{x,y} W(x,y) |\nabla P(x,y) - \nabla T(x,y)| \quad (\text{A.14})$$

where  $\nabla(\cdot)$  denotes the Sobel operator. It is a gradient-based discrete differentiation filter that estimates local intensity variations for edge detection. In our implementation, we first apply reflect padding to the input image and then convolve it with two  $3 \times 3$  Sobel kernels to obtain  $x$  and  $y$  derivative approximations.

Perceptual consistency is promoted through the Structural Similarity Index Measure (SSIM) loss

$$\mathcal{L}_{\text{SSIM}} = \frac{1}{N} \sum_{x,y} W(x,y) [1 - \text{SSIM}(P, T)] \quad (\text{A.15})$$

The multiplicative structure of Eq. (A.10) ensures that the Gaussian prior  $W_g$  and boundary emphasis  $W_b$  jointly modulate the contribution of each pixel to all loss terms. Regions near the radar centre or containing strong reflectivity receive proportionally larger gradients, while uniform or peripheral regions are downweighted. This spatially adaptive weighting scheme effectively directs learning toward the most informative regions of the radar field while maintaining stable optimisation dynamics. Empirically, it enhances the preservation of fine-scale boundaries and high-intensity features, resulting in sharper and more physically coherent reflectivity reconstructions.

#### Appendix A.2. The structure of $\mathbf{B}$ -matrix

This single-observation experiment is designed to isolate and interpret the local response of the 3DVar system to an individual radar reflectivity observation  $y_{\text{obs}}$ . This configuration provides a clean diagnostic of how the background-error covariance matrix  $\mathbf{B}$  spreads and balances the information from a single observation in the analysis field.

The 3DVar problem (Eq. (2)) is then reformulated as follows:

$$\mathcal{J}(\mathbf{x}) = \frac{1}{2} (\mathbf{x} - \mathbf{x}_b)^T \mathbf{B}^{-1} (\mathbf{x} - \mathbf{x}_b) + \frac{(y_{\text{obs}} - \mathbf{m}^T \mathcal{H}(\mathbf{x}))^2}{2\sigma_o^2} \quad (\text{A.16})$$

where  $y_{\text{obs}}$  is a scalar observation,  $\sigma_o$  its error standard deviation,  $\mathbf{m}^T$  is a row vector containing zeros and a single element with value of 1 representing the observed point, ensuring that a scalar model value is compared to a single observation. Additionally, we reformulate the gradient of the cost function as

$$\nabla \mathcal{J}(\mathbf{x}) = \mathbf{B}^{-1} (\mathbf{x} - \mathbf{x}_b) - \mathbf{M}_{\text{loc}} \left( \frac{\partial (\mathbf{m}^T \mathcal{H}(\mathbf{x}))}{\partial \mathbf{x}} \right)^T \frac{y_{\text{obs}} - \mathbf{m}^T \mathcal{H}(\mathbf{x})}{\sigma_o^2} \quad (\text{A.17})$$

where  $\mathbf{M}_{\text{loc}}$  is a binary mask matrix, which ensures that the observational part of the gradient only affects the state vector  $\mathbf{x}$  variables in grid point collocated with the observation point.

This masking strategy serves as an explicit localisation: it prevents the convolutional structure of the NN-based operator from propagating the effect of a single radar pixel across the entire radar disc (defined by the black circle in Fig. A.13).

The resulting analysis increments for a single observation extracted from the observed field of 5 August 2023 at 00UTC are shown in Fig. A.13

Horizontally, all variables exhibit a compact, nearly isotropic increment centred on the observation location, with amplitudes that smoothly decay to zero with distance. This pattern is fully consistent with the specification of the background-error covariance: the first-order RF imposes a Gaussian-like horizontal autocorrelation structure, so the information from the single pixel is spread only over a limited radius (10 Km).

Vertically and across variables, the increments illustrate how the NN-based observation operator couples the radar reflectivity to the thermodynamic and dynamical fields. Low-level humidity and 2m temperature are increased in the vicinity of the observation, while mean sea-level pressure decreases, producing a localised surface low. Temperature and wind increments exhibit level-dependent signs and magnitudes, indicating that the single reflectivity value constrains not only the moisture field but also the column structure and the local flow. Importantly, these patterns remain local and smoothly varying, confirming that the combination of the localisation mask and the RF-based background covariance effectively prevents the convolutional structure of the NN-based observation operator from generating unrealistic, domain-wide adjustments from a single observation.

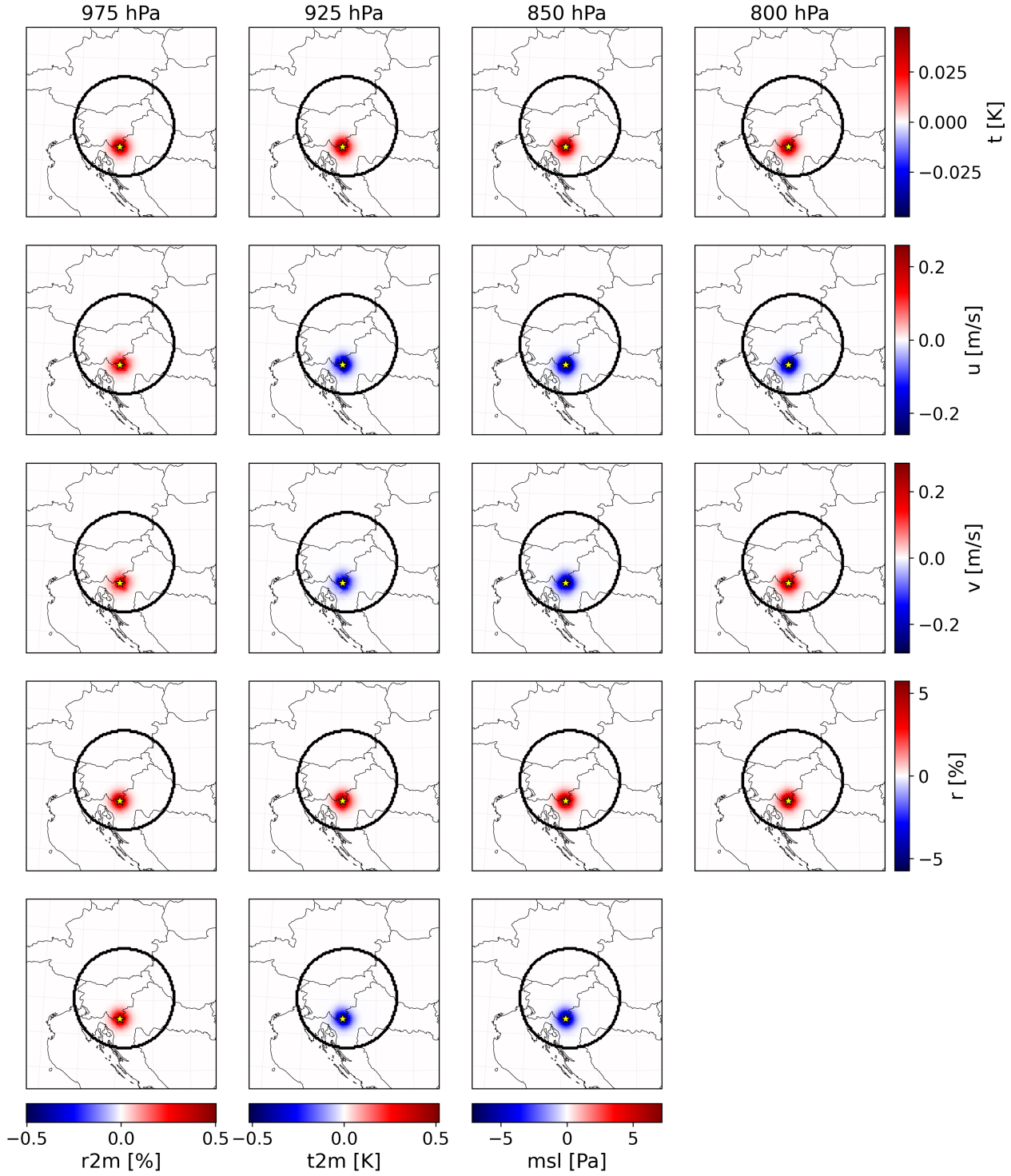


Figure A.13: Single-observation 3DVar analysis increments for the experiment of 5 August 2023 at 00 UTC. Each panel shows the increment of temperature ( $t$ ), meridional wind ( $v$ ), zonal wind ( $u$ ), relative humidity ( $r$ ) at four pressure levels (975 hPa, 925 hPa, 850 hPa, and 800 hPa), and surface fields (2 m relative humidity  $r_{2m}$ , 2 m temperature  $t_{2m}$ , and mean sea-level pressure  $msl$ ). The increments are obtained by assimilating a single radar reflectivity observation. The black circle denotes the radar disc.